Sets of rotation-aligned bands indicating nonaxiality in ^{190}Au

E. Gueorguieva,[1,2,3,*] C. Schück,[1] A. Minkova,[2] Ch. Vieu,[1] M. Kaci,[4] F. Hannachi,[1] R. Wyss,[5] J. S. Dionisio,[1] A. Korichi,[1] and A. Lopez-Martens[1]
[1]*CSNSM CNRS-IN2P3, F-91405 Orsay, France*
[2]*Faculty of Physics, University of Sofia, "St. K. Ohridski," Sofia 1164, Bulgaria*
[3]*iThemba Laboratory for Accelerator Based Sciences, P.O. Box 722, 7129 Somerset West, South Africa*
[4]*IFIC, Edificio Institutos de Paterna, Apartado Postal 22085, ES-46071 Valencia, Spain*
[5]*Royal Institute of Technology, Frescativägen 24, S-10405 Stockholm, Sweden*
(Received 14 January 2004; published 28 April 2004)

The level scheme of ^{190}Au was extended up to high spin using γ spectroscopy with the Eurogam-II array and internal conversion measurements with the electron-γ spectrometer of Orsay. Several sets of rotation-aligned bands were found and associated with high-j, low-K configurations. According to the total Routhian surface and cranked shell model calculations these bands are caused by the nonaxiality of the nuclear deformation ($\gamma \lesssim -70°$). Furthermore, very good agreement was obtained between the experimental data and the theoretical predictions for the properties of these bands, such as alignments, band-crossing frequencies, and signature inversion, thus supporting the suggested nonaxial shapes.

DOI: 10.1103/PhysRevC.69.044320 PACS number(s): 23.20.Lv, 21.60.Ev, 27.80.+w, 29.30.Kv

I. INTRODUCTION

The $_{78}$Pt, $_{79}$Au, and $_{80}$Hg isotopes in the $A=190$ region are moderately deformed with oblate shape and $\beta_2 \lesssim 0.16$ [1–5]. They show rotational bands built on different multi-quasiparticle excitations [6]. The properties of the low spin states in these nuclei have been studied in several works and nonaxiality of the nuclear shape was suggested [4,5,7].

Two-quasiparticle $\pi h_{11/2}^{-1} \otimes \nu i_{13/2}^{-1}$ rotational bands are known in the odd-odd ^{190,192,194}Au nuclei [8]. Although these bands look like strongly coupled bands (built of $M1$ direct and $E2$ crossover transitions) they were associated with a low-K configuration and interpreted using rigid triaxial rotor calculations as a set of rotation-aligned bands, formed by the coupling of two rotation-aligned quasiparticles to a slightly deformed nonaxially symmetric Hg core [8,9]. The configurations for which such sets of rotation-aligned bands can be expected in the $A=190$ Pt-Au-Hg isotopes were studied [10] with the total Routhian surface (TRS) [11,12] and cranked shell model (CSM) calculations using universal Woods-Saxon potential [13]. The calculations predicted that a hole in the $\pi h_{11/2}$ and/or $\nu h_{9/2}$ shells could induce triaxial deformation with $\gamma \lesssim -80°$. Furthermore, at such nonaxiality the signature splitting of the A, B, and C Routhians (originating from low-K $\nu i_{13/2}$ orbitals) becomes small and the B Routhian becomes yrast. Thus, one (or two) excited neutron(s) can occupy any of the three A, B, or C (AB, BC, or AC) Routhians, which results in a set of up to three rotation-aligned bands. In the case of three excited neutrons, however, the three close lying positive parity Routhians will be occupied and thus only one band is expected. These predictions were found in very good agreement with the available experimental data in several nuclei in this mass region [10].

In this work the doubly odd ^{190}Au nucleus is studied up to high spins in order to compare the theoretical predictions for such sets of rotation-aligned bands with the experimental data.

II. EXPERIMENTAL PROCEDURE

γ spectroscopy and internal conversion spectroscopy experiments were performed in order to study ^{190}Au. The γ experiment was carried out with the Eurogam-II multidetector array [14,15], operated at the Vivitron accelerator in Strasbourg. The ^{186}W(^{11}B, 7n) reaction at beam energies of 84 and 86 MeV, and a self-supporting target of two 280 μg/cm^2 foils were used. The trigger required five or more unsuppressed detectors to fire in coincidence. The resulting data set consisted of $\sim 9 \times 10^8$ fourfold and higher-fold events. In this fusion-evaporation reaction the major products, ^{190}Au and ^{191}Au, were produced with relative yields of 51% and 37% of the total cross section, respectively. The results relating to ^{191}Au were reported previously [10,16].

The analysis of the data involved (i) a study of the γ coincidence relationships using an E_γ-E_γ-E_γ cube and different gated matrices, (ii) angular distribution and linear polarization measurements in order to deduce the spins and parities of the levels, (iii) γ-intensity measurements, and (iv) a search for nanosecond isomers using the recoil shadow anisotropy method [17]. More details about the data analysis can be found in Ref. [18].

A complementary internal conversion spectroscopy experiment was performed using the electron-γ spectrometer at the Orsay tandem accelerator. The aim of this experiment was to assist in the measurement of transition multipolarities, in particular for low energy transitions. The electron spectrometer consisted of a Kleinheinz magnetic lens with transmission $T=(4.11\pm0.15)\times10^{-2}$ and momentum window $\Delta B\rho/B\rho=30\%$, coupled to a large composite cooled Si(Li) detector (area: 2×7.5 cm^2) [19]. The spectrometer was set at 90° relative to the beam direction. The current in the mag-

*Email address: elena@tlabs.ac.za

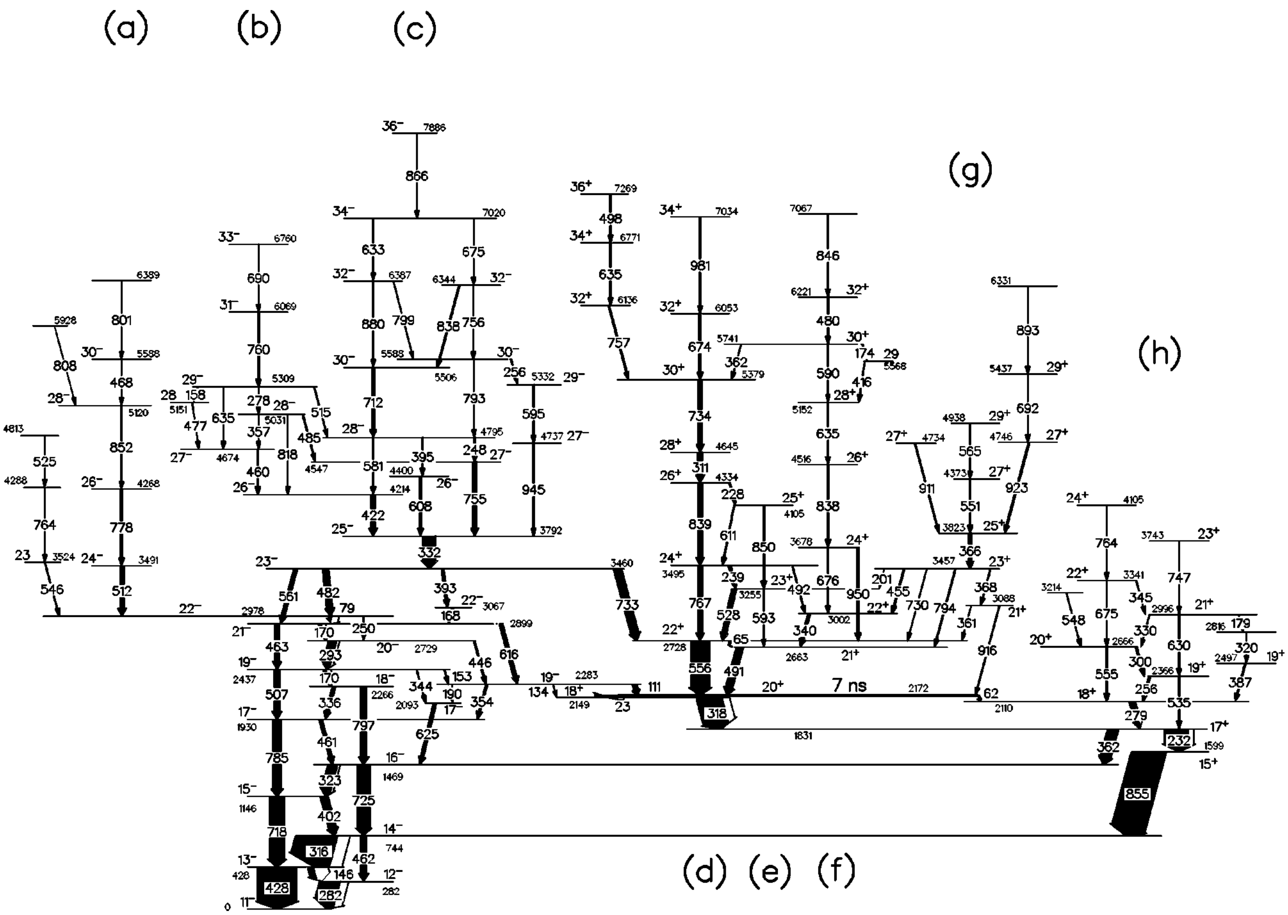

FIG. 1. Level scheme of ^{190}Au obtained from this work. The width of the arrows represent the intensity of the transitions.

netic lens was chosen to sweep within an interval allowing detection of electrons in the energy range 30–350 keV. Eight Compton-suppressed Eurogam-I Ge detectors (80% efficiency) were mounted in the hemisphere opposite to the electron spectrometer. In addition, six BaF_2 detectors were mounted around the target. The ^{190}Au nuclei were produced using the reaction $^{184}W(^{11}B,5n)^{190}Au$ with a pulsed ^{11}B beam of 70 MeV, and with a 500 $\mu g/cm^2$ target, set at 45° relative to the beam direction. The trigger was set to accept events when at least one BaF_2 and one Ge detector fired in coincidence with a Si(Li) detector or another Ge detector and the beam burst.

Two asymmetric matrices, $E_\gamma(90°)-E_\gamma$ and $E_{e^-}-E_\gamma$, were built. The internal conversion coefficients were measured using the electron and γ spectra obtained after setting the same gate on the E_γ axis of both matrices. Lifetime measurements were performed by measuring the slope of the time distribution of the electron lines for the isomeric transitions.

III. RESULTS

The previously known level scheme [8,20] was considerably extended up to an excitation energy of ~7.9 MeV and spin of 36$\hbar$, as shown in Fig. 1. The obtained transition energies, γ intensities, angular distribution coefficients, polarization asymmetry, and internal conversion coefficients are listed in Table I. The data analysis allowed unambiguous determination of the spin and parity of most of the new levels. A partial level scheme obtained from this work was previously published in Ref. [18].

A. Negative parity states

The 11^- and 12^- bands were extended up to the 22^- level at 2978 keV. The energy of the new 79-keV transition $(22^- \rightarrow 21^-)$ coincides with the energy of the K_β x rays of Au. This transition was identified using the spectra shown in Fig. 2. The spectrum double gated on the 332- and 482-keV lines shows the same coincidence relationships as the spectrum double gated on the 332- and 561-keV γ rays, except that the K_β line appears to be much stronger than the K_α line indicating the presence of a 79-keV γ ray. Furthermore, the spectrum double gated on the 332- and 79-keV transitions shows strong coincidence with the 482-keV transition and similar other coincidence relationships. Thus, a new 79-keV transition was placed to connect the 22^- and 21^- levels, in anticoincidence with the 561-keV transition. In the complementary internal conversion coefficient experiment the *M* line of this transition could be observed in the electron spectra (as shown in Fig. 3). It should be noted that the *L* internal conversion line of this transition is strongly mixed with the *K* line of the 146-keV transition.

TABLE I. Energy, γ intensity, angular distribution coefficients, linear polarization asymmetry, measured K conversion coefficients, and deduced multipolarity of the transition in ^{190}Au. The spin assignments and the energies of the initial levels are also included. I_γ and I_{tot} are normalized to the intensity of the 232-keV transition. The multipolarity ML is given if the a_2 and a_4 coefficients and either the polarization asymmetry of the K conversion coefficient were measured.

E_γ (keV)	I_γ	a_2	a_4	A_{pol}	α_k(exp)	ML	I_{tot}	E_i (keV)	$I_i^\pi \to I_f^\pi$
23.1(5)[a]								2172	$20^+ \to 18^+$
62.0(5)[a]								2172	$20^+ \to 18^+$
65.1(5)[a]							6[a]	2728	$22^+ \to 21^+$
79.2(4)					0.30(14)[b]	$M1$	34[a]	2978	$22^- \to 21^-$
111.1(2)	11(1)	−0.68(4)	0.3(1)		0.042(10)[b]	$E1$	15	2283	$19^- \to 20^+$
134.2(3)	0.8(3)	−0.3(2)	0.1(1)				1	2283	$19^- \to 18^+$
145.5(2)	19(2)	−0.42(6)	0.07(8)		1.4(3)	$M1$	69	428	$13^- \to 12^-$
152.8(3)	0.7(2)	0.2(2)	0.2(1)				2.5	2437	$19^- \to 19^-$
158.2(3)	0.2(1)							5309	$29^- \to 28$
167.8(4)	2.7(5)	−0.5(1)	0.1(2)		1.5(6)	$M1$	7	3067	$22^- \to 21^-$
170.2(3)	9(2)	−0.31(4)[c]	0.05(8)[c]		1.4(3)	$M1$	24	2899	$21^- \to 20^-$
170.4(4)	10(2)	−0.31(4)[c]	0.05(8)[c]		1.5(2)	$M1$	26	2437	$19^- \to 18^-$
173.5(4)	1.1(3)						2.8	5741	$30^+ \to 29$
179.0(4)	0.2(1)						0.4	2996	$21^+ \to$
190.2(3)	0.3(1)	0.2(1)	0.09(8)		0.37(11)	$E2$	3.5	2283	$19^- \to 17^-$
201.3(4)	0.3(1)	0.4(1)	0.03(8)				0.6	3457	$23^+ \to 23^+$
228.0(3)	2.3(3)	−0.27(8)	0.02(8)		0.57(14)	$M1$	4	4334	$26^+ \to 25^+$
232.3(2)	81	0.21(4)	−0.08(8)	+0.106(22)	0.14(1)	$E2$	100	1831	$17^+ \to 15^+$
238.9(2)	6(1)	−0.3(2)	−0.01(8)		0.67(8)	$M1$	10	3495	$24^+ \to 23^+$
247.6(3)	5(1)	−0.21(6)	−0.09(8)				7	4795	$28^- \to 27^-$
249.6(4)	3(1)	0.3(1)	0.10(8)				3.6	2978	$22^- \to 20^-$
255.7(4)	4(1)	−0.24(6)	−0.06(8)		0.60(10)	$M1$	5.5	2366	$19^+ \to 18^+$
256.0(3)	1.8(4)	−0.3(1)	−0.09(8)				2.8	5588	$30^- \to 29^-$
277.7(3)	1.0(4)	−0.1(1)	−0.15(8)		0.53(19)	$M1$	1.4	5309	$29^- \to 28^-$
279.3(3)	15(2)	−0.07(8)	0.08(8)		0.36(4)	$M1$	22	2110	$18^+ \to 17^+$
282.0(2)	68(8)	−0.11(4)	−0.09(8)	−0.079(14)	0.39(3)	$M1$	96	282	$12^- \to 11^-$
292.6(2)	27(3)	−0.09(4)	−0.07(8)	−0.076(16)	0.36(3)	$M1$	37	2729	$20^- \to 19^-$
299.6(4)	4(1)	−0.02(8)	0.01(8)				5	2666	$20^+ \to 19^+$
311.1(2)	15(3)	0.23(4)	−0.07(8)	+0.100(7)	0.097(50)	$E2$	15	4645	$28^+ \to 26^+$
315.7(3)	138(12)	−0.05(4)	−0.06(8)	−0.071(8)[c]	0.26(2)	$M1$	179	744	$14^- \to 13^-$
318.2(2)	85(10)	−0.10(4)	−0.08(8)	−0.071(8)[c]	0.23(2)	$M1$	111	2149	$18^+ \to 17^+$
319.5(3)	0.9(3)	0.3(1)	0.16(8)				1.2	2816	$\to 19^+$
322.8(2)	32(3)	−0.04(4)	−0.05(8)	−0.040(18)	0.20(5)	$M1$	41	1469	$16^- \to 15^-$
329.8(3)	1.3(4)	−0.1(1)	0.00(8)				1.7	2996	$21^+ \to 20^+$
332.2(2)	41(3)	0.25(4)	−0.14(8)	+0.113(12)	0.035(6)	$E2$	44	3792	$25^- \to 23^-$
335.6(2)	9(1)	0.01(4)	−0.03(8)	−0.064(24)	0.18(3)	$M1$	11	2266	$18^- \to 17^-$
339.7(2)	7(1)	−0.14(4)	−0.16(8)	−0.76(9)	0.11(3)	$M1$	9	3002	$22^+ \to 21^+$
343.6(5)	1.9(4)	0.47(8)	−0.20(8)				2	2437	$19^- \to 17^-$
345.4(5)	1.4(5)	−0.1(1)	−0.17(8)				1.7	3341	$22^+ \to 21^+$
353.6(4)	6(2)	0.2(1)	0.05(8)		0.066(18)	$E2$	6	2283	$19^- \to 17^-$
357.0(4)	0.8(4)						1	5031	$28^- \to 27^-$
361.1(3)	0.6(2)	−0.2(1)	−0.39(8)				0.7	3088	$21^+ \to 22^+$
362.0(3)	1.1(4)	0.4(2)	−0.02(8)				1.3	5741	$30^+ \to 30^+$
362.3(2)	36(3)	−0.29(4)	−0.04(8)	+0.003(16)	0.011(2)	$E1$	37	1831	$17^+ \to 16^-$
365.7(2)	11(1)	0.31(4)	−0.25(8)	+0.124(7)	0.031(9)	$E2$	12	3823	$25^+ \to 23^+$
368.4(3)	2.3(5)	0.14(6)	−0.33(8)	+0.153(15)		$E2$	2.4	3457	$23^+ \to 21^+$

TABLE I. (*Continued.*)

E_γ (keV)	I_γ	a_2	a_4	A_{pol}	α_k(exp)	ML	I_{tot}	E_i (keV)	$I_i^\pi \rightarrow I_f^\pi$
386.5(3)	3.5(6)	0.03(8)	−0.07(8)		0.20(6)	$M1$	3.7	2497	$19^+ \rightarrow 18^+$
392.7(3)	7(1)	−0.07(8)	−0.04(8)	−0.024(18)	0.23(5)	$M1$	8	3460	$23^- \rightarrow 22^-$
394.5(4)	2.4(8)	0.4(1)	−0.24(8)	+0.093(16)		$E2$	2.5	4795	$28^- \rightarrow 26^-$
402.0(2)	23(2)	−0.21(4)	−0.07(8)	−0.039(17)	0.13(2)[d]	$M1$	27	1146	$15^- \rightarrow 14^-$
416.1(4)	1.9(4)	−0.2(1)	−0.2(1)				2.2	5568	$29 \rightarrow 28^+$
421.8(2)	15(2)	0.03(4)	−0.00(8)	−0.100(49)	0.19(3)[d]	$M1$	17.6	4214	$26^- \rightarrow 25^-$
427.8(2)	128(10)	0.25(4)	−0.09(8)	+0.053(8)	0.026(2)[d]	$E2$	146	428	$13^- \rightarrow 11^-$
445.7(2)	4(1)	−0.2(1)	0.05(8)				4.5	2729	$20^- \rightarrow 19^-$
454.6(3)	3.6(7)	0.00(4)	−0.03(8)		0.11(2)[d]	$M1$	4	3457	$23^+ \rightarrow 22^+$
460.2(5)	4.5(9)	−0.12(4)[c]	−0.04(8)[c]				5	4674	$27^- \rightarrow 26^-$
461.4(5)	10(3)	−0.12(4)[c]	−0.04(8)[c]		0.043(2)[c,d]	$M1$	11	1930	$17^- \rightarrow 16^-$
461.8(4)	20(2)	0.24(6)	−0.36(8)	+0.038(10)	0.043(2)[c,d]	$E2$	21	744	$14^- \rightarrow 12^-$
462.7(5)	16(4)			+0.022(9)			16.5	2899	$21^- \rightarrow 19^-$
467.6(3)	0.7(2)	0.7(1)	−0.2(1)				0.7	5588	$30^- \rightarrow 28^-$
476.5(4)	1.1(4)	−0.1(1)	−0.08(8)				1.2	5151	$28 \rightarrow 27^-$
479.5(4)	3.1(8)	0.2(1)	−0.21(8)				3.2	6221	$32^+ \rightarrow 30^+$
481.5(3)	19(2)	−0.22(4)	−0.08(8)	−0.045(10)	0.058(4)[d]	$M1$	21	3460	$23^- \rightarrow 22^-$
484.8(4)	2.7(5)	−0.0(1)	−0.12(8)	−0.077(14)		$M1$	3	5031	$28^- \rightarrow 27^-$
490.5(2)	22(2)	0.08(4)	−0.04(8)	−0.067(8)	0.048(2)[d]	$M1$	24	2663	$21^+ \rightarrow 20^+$
492.0(5)	2.5(7)	0.1(1)[c]	−0.09(8)[c]				2.6	3495	$24^+ \rightarrow 22^+$
498.2(2)	2.7(4)	0.2(1)	−0.13(8)				2.8	7269	$36^+ \rightarrow 34^+$
506.6(2)	20(2)	0.22(4)	−0.16(8)	+0.102(14)		$E2$	21	2437	$19^- \rightarrow 17^-$
512.1(2)	15(2)	0.32(4)	−0.17(8)	+0.074(8)		$E2$	15	3491	$24^- \rightarrow 22^-$
514.8(3)	1.9(5)	−0.3(1)	0.06(8)				2	5309	$29^- \rightarrow 28^-$
524.8(4)	1.3(4)						1.3	4813	
528.1(2)	15(2)	0.02(4)	−0.08(8)	−0.070(10)		$M1$	16	3255	$23^+ \rightarrow 22^+$
535.2(3)	3.5(8)	0.31(6)	−0.2(1)	+0.254(13)		$E2$	3.6	2366	$19^+ \rightarrow 17^+$
545.6(3)	2.0(5)	−0.4(1)	0.08(8)				2.1	3524	$23 \rightarrow 22^-$
548.3(3)	1.3(4)						1.3	3214	$\rightarrow 20^+$
550.6(2)	5(1)	0.21(6)	0.04(8)				5.3	4373	$27^+ \rightarrow 25^+$
555.3(4)	6(2)						6	2666	$20^+ \rightarrow 18^+$
555.6(2)	63(5)	0.23(4)	−0.08(8)	+0.076(9)		$E2$	64	2728	$22^+ \rightarrow 20^+$
560.6(2)	12(2)	0.4(1)	−0.2(1)	+0.065(12)		$E2$	12	3460	$23^- \rightarrow 21^-$
565.1(4)	2.0(5)	0.56(8)	−0.33(8)				2	4938	$29^+ \rightarrow 27^+$
580.8(2)	5(1)	0.38(6)	−0.2(1)	+0.126(10)		$E2$	5	4795	$28^- \rightarrow 26^-$
589.7(5)	0.9(4)						0.9	5741	$30^+ \rightarrow 28^+$
592.7(5)	2.0(5)						2	3255	$23^+ \rightarrow 21^+$
595.3(5)	3(1)						3	5332	$29^- \rightarrow 27^-$
608.0(3)	6(2)	−0.26(4)	0.1(1)				6	4400	$26^- \rightarrow 25^-$
610.8(2)	3(1)	−0.16(8)	0.17(8)				3	4105	$25^+ \rightarrow 24^+$
615.9(2)	12(2)	0.20(4)	−0.09(8)	+0.118(16)	0.012(2)[d]	$E2$	12	2899	$21^- \rightarrow 19^-$
624.7(3)	10(2)	−0.06(8)	0.4(1)				10	2093	$17^- \rightarrow 16^-$
629.8(3)	3(1)	0.3(1)	0.12(8)				3	2996	$21^+ \rightarrow 19^+$
633.4(3)	1.8(6)	0.4(1)	−0.05(8)	+0.048(10)[c]		$E2$	1.8	7020	$34^- \rightarrow 32^-$
634.6(3)	3.5(5)	0.4(1)	−0.01(8)				3.6	6771	$34^+ \rightarrow 32^+$
634.8(3)	2.2(3)	0.28(8)	−0.06(8)	+0.048(10)[c]		$E2$	2.2	5309	$29^- \rightarrow 27^-$
635.1(4)	2.0(6)	0.39(8)	−0.34(8)				1	5152	$28^+ \rightarrow 26^+$
673.5(3)	7(1)	0.23(8)	0.14(8)	+0.081(6)[c]		$E2$	7	6053	$32^+ \rightarrow 30^+$

TABLE I. (*Continued.*)

E_γ (keV)	I_γ	a_2	a_4	A_{pol}	α_k(exp)	ML	I_{tot}	E_i (keV)	$I_i^\pi \rightarrow I_f^\pi$
675.2(5)	2.6(5)	0.3(1)	−0.14(8)	+0.081(6)[c]		$E2$	2.6	3341	$22^+ \rightarrow 20^+$
675.3(3)	1.7(3)	0.3(1)	−0.23(8)				1.7	7020	$34^- \rightarrow 32^-$
675.6(4)	2.5(8)	0.41(8)	−0.38(8)	+0.081(6)[c]		$E2$	2.5	3678	$24^+ \rightarrow 22^+$
690.4(4)	1.3(4)	0.3(1)	−0.5(12)				1.3	6760	$33^- \rightarrow 31^-$
691.5(5)	2.8(7)	0.22(6)	−0.04(8)				2.8	5437	$29^+ \rightarrow 27^+$
711.8(2)	10(2)	0.38(6)	−0.03(8)	+0.092(7)		$E2$	10	5506	$30^- \rightarrow 28^-$
717.7(2)	51(5)	0.17(4)	−0.12(8)	+0.068(10)		$E2$	52	1146	$15^- \rightarrow 13^-$
724.7(2)	44(4)	0.27(4)	−0.14(8)	+0.061(11)		$E2$	44	1469	$16^- \rightarrow 14^-$
729.5(4)	1.1(3)						1.1	3457	$23^+ \rightarrow 22^+$
732.5(2)	27(2)	−0.28(4)	0.5(1)	+0.043(8)		$E1$	27	3460	$23^- \rightarrow 22^+$
734.3(2)	13(3)	0.29(4)	−0.18(8)	+0.056(7)		$E2$	3	5379	$30^+ \rightarrow 28^+$
746.5(4)	1.2(4)	0.3(2)	−0.20(8)				1.2	3743	$23^+ \rightarrow 21^+$
754.8(3)	14(1)	0.24(4)	−0.19(8)	+0.096(5)		$E2$	14	4547	$27^- \rightarrow 25^-$
756.3(4)	1.7(5)						1.7	6344	$32^- \rightarrow 30^-$
756.5(3)	4(1)	0.49(6)	−0.04(8)				4	6136	$32^+ \rightarrow 30^+$
760.2(4)	5(1)	0.25(8)	−0.26(8)	+0.077(10)		$E2$	5	6069	$31^- \rightarrow 29^-$
764.2(4)	1.4(3)	0.5(1)	−0.25(8)				1.4	4105	$24^+ \rightarrow 22^+$
764.2(3)	1.2(3)						1.2	4288	$\rightarrow 23$
767.0(2)	15(2)	0.25(4)	−0.11(8)	+0.069(11)		$E2$	15	3495	$24^+ \rightarrow 22^+$
777.7(2)	6(2)	0.53(6)	−0.1(1)	+0.161(14)		$E2$	6	4268	$26^- \rightarrow 24^-$
784.5(2)	29(2)	0.18(4)	−0.16(8)	+0.064(12)		$E2$	29	1930	$17^- \rightarrow 15^-$
793.0(4)	1.3(4)						1.3	5588	$30^- \rightarrow 28^-$
794.1(3)	3.1(4)	0.28(4)	−0.11(8)				3.1	3457	$23^+ \rightarrow 21^+$
797.0(2)	22(2)	0.21(4)	−0.2(1)	+0.066(14)		$E2$	22	2266	$18^- \rightarrow 16^-$
798.8(3)	1.1(3)	0.6(1)	−0.2(1)				1.1	6387	$32^- \rightarrow 30^-$
801.3(4)	0.2(1)						0.2	6389	$\rightarrow 30^-$
808.2(4)	0.4(1)						0.4	5928	$\rightarrow 28^-$
817.8(4)	1.8(8)	0.10(4)	−0.67(8)				1.8	5031	$28^- \rightarrow 26^-$
837.5(4)	4(1)	0.32(6)	0.13(8)				4	6344	$32^- \rightarrow 30^-$
838.3(4)	6(2)	0.28(6)	−0.26(8)				6	4516	$26^+ \rightarrow 24^+$
839.1(3)	15(2)	0.23(4)	−0.09(8)	+0.108(10)		$E2$	15	4334	$26^+ \rightarrow 24^+$
845.8(5)	2.0(5)						2	7067	$\rightarrow 32^+$
849.6(5)	6(3)						6	4105	$25^+ \rightarrow 23^+$
851.8(4)	3(1)	0.4(1)	−0.2(1)				3	5120	$28^- \rightarrow 26^-$
854.9(3)	115(10)	−0.11(4)	−0.07(8)	+0.018(3)		$E1$	115	1599	$15^+ \rightarrow 14^-$
866.3(3)	2.0(4)	0.27(8)	−0.02(8)	+0.122(11)		$E2$	2	7886	$36^- \rightarrow 34^-$
880.3(3)	2.1(4)	0.4(1)	0.05(8)				2.1	6387	$32^- \rightarrow 30^-$
893.4(3)	2.1(5)						2.1	6331	$\rightarrow 29^+$
911.4(3)	3(1)	0.23(8)	−0.34(8)				3	4734	$27^+ \rightarrow 25^+$
916.2(4)	2.0(6)	−0.42(8)	0.02(8)				2	3088	$21^+ \rightarrow 20^+$
923.4(3)	5(1)	0.30(6)	−0.07(8)				5	4746	$27^+ \rightarrow 25^+$
944.6(4)	3(1)	0.24(8)	−0.08(8)				3	4737	$27^- \rightarrow 25^-$
950.1(4)	8(3)	0.27(6)	−0.14(8)				8	3678	$24^+ \rightarrow 22^+$
981.4(4)	3(1)	0.5(1)	−0.06(8)				3	7034	$34^+ \rightarrow 32^+$

[a]Deduced from the coincidence relationships.
[b]The values for the 79- and 111-keV transitions correspond to α_M and α_L conversion coefficients, respectively.
[c]Nonseparated doublet or triplet. The value corresponds to the total peak.
[d]Deduced in direct (ungated) internal conversion measurements, e.g., using the electron spectra and the γ spectra of the Ge detector at 90° measured in coincidence with the beam burst and at least one BaF_2 detector.

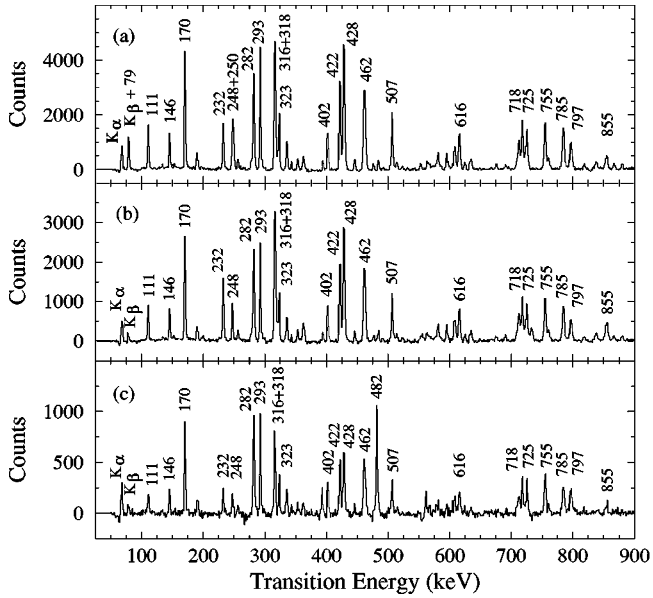

FIG. 2. Spectra double gated on the 332-keV transition and (a) 482-, (b) 561-, and (c) 79-keV γ rays.

A new sequence of $E2$ transitions labeled (a) was found to develop above the 22^- level at 2978 keV. The coincidence of the 512-keV transition with the 79- and 250-keV lines determined the placement of this band above the 22^- level. A few weak transitions (546, 764, and 525 keV) were found to lie parallel to this band. Their multipolarities, however, could not be determined. The most intense new structure with negative parity, labeled (c), is built above the 23^- level at 3460 keV and consists of $E2$ and $M1$ transitions. It develops up to the 36^- level at 7.89 MeV, which is the highest energy level observed in this nucleus. Another new structure, labeled (b), consists of $M1$ and $E2$ transitions and feeds the lower lying levels of structure (c).

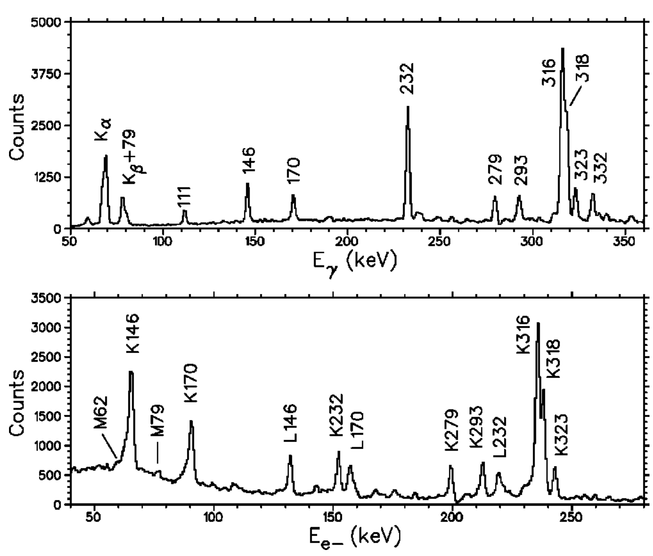

FIG. 3. γ (upper panel) and electron (lower panel) spectra, gated on the 282-keV transition, obtained from the internal conversion spectroscopy experiment.

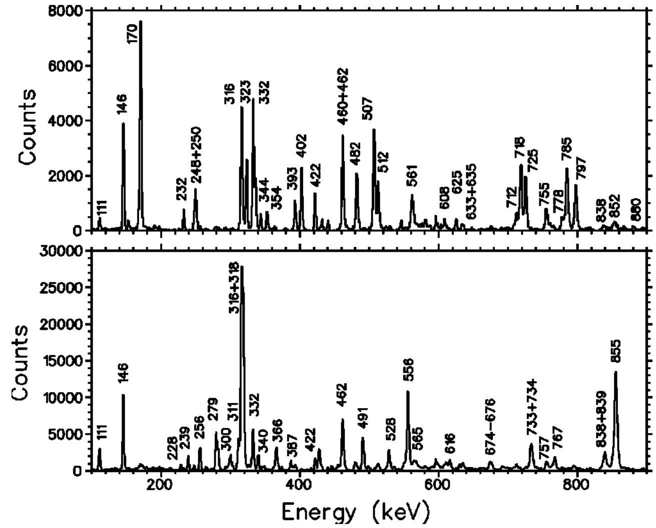

FIG. 4. Top panel: Spectra double gated on the 282- and 293-keV γ rays, showing the transitions from the negative parity structures. Bottom panel: Spectra double gated on the 282- and 232-keV γ rays, showing the transitions from the positive parity structures.

A spectrum double gated on the 282- and 293-keV γ rays, showing the transitions from the negative parity structures in ^{190}Au, is plotted in the top panel of Fig. 4.

B. Positive parity states

New positive parity structures were found in ^{190}Au and several already known ones were extended to higher spin. A new 20^+ level at 2172 keV was introduced, which deexcites towards the previously known 18^+ level at 2149 keV by a 23-keV transition and towards a new 18^+ level at 2110 keV by a 62-keV transition. Using the recoil shadow anisotropy method [17] with the Eurogam-II data, and the time spectrum of the electron lines with the internal conversion spectroscopy data, the 20^+ level was found to be isomeric with a half-life of 7.0 ± 0.3 ns. More details about the identification and the lifetime measurements of this isomeric state were published in Ref. [18].

The previously known sequences (d) and (g) [20] were extended and a new sequence of $E2$ transitions labeled (f) was found. The sequence (e), consisting of the 593- and 850-keV transitions was previously known [20]. A new structure labeled (h) consists of $M1$ and $E2$ transitions and develops above the previously known 17^+ level at 1831 keV [8].

A spectrum double gated on the 282- and 232-keV γ rays showing the transitions from the positive parity structures in ^{190}Au is plotted in the bottom panel of Fig. 4.

IV. DISCUSSION

It is known that the coupling of the high-j low-K quasiparticles in the $A=190$ Pt-Au-Hg isotopes leads either to decoupled bands or to sets of rotation-aligned bands [6]. The configurations and properties of the latter were recently pre-

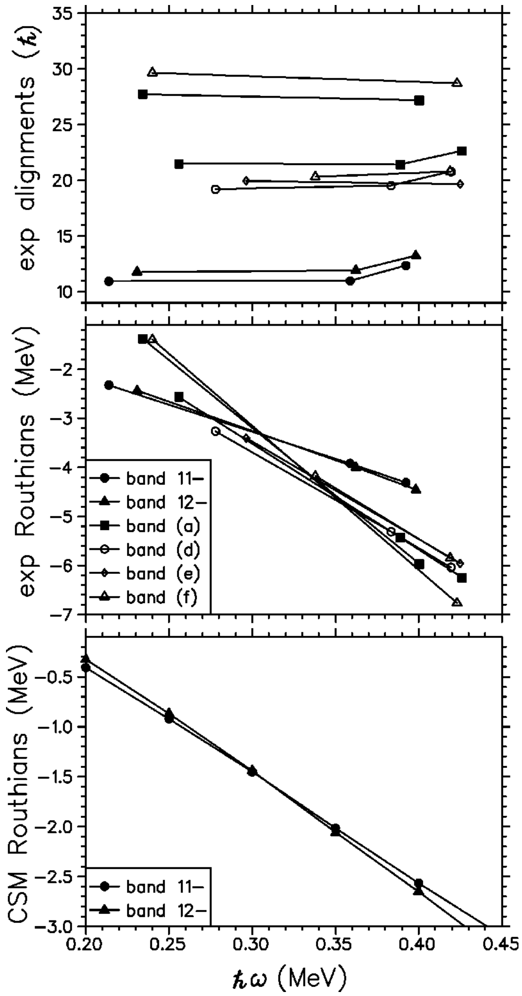

FIG. 5. Experimental alignments (upper panel) and Routhians (middle panel) for the bands in ^{190}Au, calculated with $K=0$ and Harris parameters of $J_0=6\,\hbar^2\mathrm{MeV}^{-1}$ and $J_1=30\hbar^4\mathrm{MeV}^{-3}$. The CSM Routhians (bottom panel) for the 11^- and 12^- bands were calculated for the predicted γ deformations of −80° and −70°, respectively.

dicted using TRS and CSM calculations [10]. The following discussion focuses on studying such high-j low-K bands in ^{190}Au and comparing them to the theoretical predictions.

The ^{190}Au nucleus is expected to have near oblate shape with moderate deformation of $\beta_2\sim 0.13$ [9]. The orbitals closest to the Fermi level for this deformation are low-K orbitals from the $\nu i_{13/2}$ and $\nu h_{9/2}$ (and/or $\nu f_{7/2}$) shells and low-j orbitals from the $\nu p_{3/2}$ and $\nu f_{5/2}$ shells, as well as low-K $\pi h_{11/2}$ orbitals (see Fig. 4 from Ref. [10]). Considering the deformation driving properties of these orbitals (as predicted by the TRS calculations), a nonaxial shape with $\gamma \lesssim -80°$ may be induced by the odd $h_{11/2}^{-1}$ proton [10]. Since for such nonaxial deformation the lowest neutron A, B, and C Routhians (originating from low-K $i_{13/2}$ orbitals) are expected to lie very close to each other, the excitation of one or two $i_{13/2}$ neutron(s) can lead to a set of rotation-aligned bands [10].

The experimental alignments and Routhians of the bands in ^{190}Au are shown in the top and middle panels of Fig. 5, respectively. The calculations used the same values of the Harris parameters of $J_0=6\hbar^2\mathrm{MeV}^{-1}$ and $J_1=30\hbar^4\mathrm{MeV}^{-3}$ as those of the neighboring ^{191}Au nucleus [10], and $K=0$ for all the bands.

TRS calculations predict nonaxial shape for several configurations in ^{190}Au, as shown in Fig. 6. CSM calculations were then performed for ^{190}Au using $\beta_2=0.137$ and $\beta_4=-0.027$, as predicted by TRS, and for γ deformation of −60°, −70°, −80°, and −90° (the neutron quasiparticle Routhians are plotted in Fig. 7). It should be noted that for large nonaxiality the lowest lying positive parity positive-signature Routhian has smaller alignment at low rotational frequency than the second lowest one, while it is the opposite for axially symmetric nuclei (see Fig. 7). Thus, in this work, the Routhian with the larger alignment is labeled A for all γ deformations and frequencies, while the one with smaller alignment is labeled C. Some information about the labeling convention as well as the aligned angular momenta and band-crossing frequencies calculated with CSM are listed in Table II.

As in the neighboring ^{191}Au nucleus [10] a constant neutron pairing gap of 1.0 MeV was used in the CSM calculations. In the ^{191}Hg isotone better agreement with the experimental measurements was obtained for several band-crossing frequencies by using configuration dependent neutron pairing gaps (ranging from 0.66 MeV to 1.15 MeV) [21]. Since much larger nonaxiality is predicted for the bands in ^{190}Au, no attempt is made here to use the configuration dependent pairing gaps of ^{191}Hg. Emphasis is rather placed on studying the differences in the experimental band-crossing frequencies in the axially symmetric ^{191}Hg and the nonaxial ^{190}Au isotones that can arise as a result of changes in the nuclear shape.

Thus, keeping these considerations in mind the predictions for the presence, alignments, band-crossing frequencies, and signature inversion in the high-j low-K bands of ^{190}Au are compared with the experimental data.

A. The 11^- and 12^- bands

The 11^- and 12^- bands were previously assigned to a rotation-aligned $\pi h_{11/2}^{-1}\otimes \nu i_{13/2}^{-1}$ configuration [8,9] (or eB and eA configurations using the CSM labels). The TRS calculations predict nonaxial deformation of $\beta_2=0.14$ and $\gamma\sim -78°$ for the 11^- sequence and the same β_2 and $\gamma\sim -70°$ for the 12^- sequence [see panels (a) and (b) in Fig. 6]. For such nonaxiality the B and A Routhians lie very close (see Figs. 7 and 5), and thus a set of rotation-aligned bands are expected in very good agreement with the experimental observations. The experimental alignments of $11\hbar$ and $12\hbar$ of the 11^- and 12^- sequences, respectively (see Fig. 5), are in good agreement with the predicted alignments of $10.7\hbar$ and $11.5\hbar$ at $\gamma=-80°$ and $\gamma=-70°$ respectively (see Table II).

Signature inversion appears in the 11^- and 12^- bands in ^{190}Au as well as in the yrast bands in the neighboring doubly odd $^{186-194}$Au nuclei [8,22]. This phenomenon is manifested by the inverted position of the experimental Routhians at low rotational frequency, i.e., the Routhian of the 11^- band (unfavored signature) lies at lower excitation energy than the

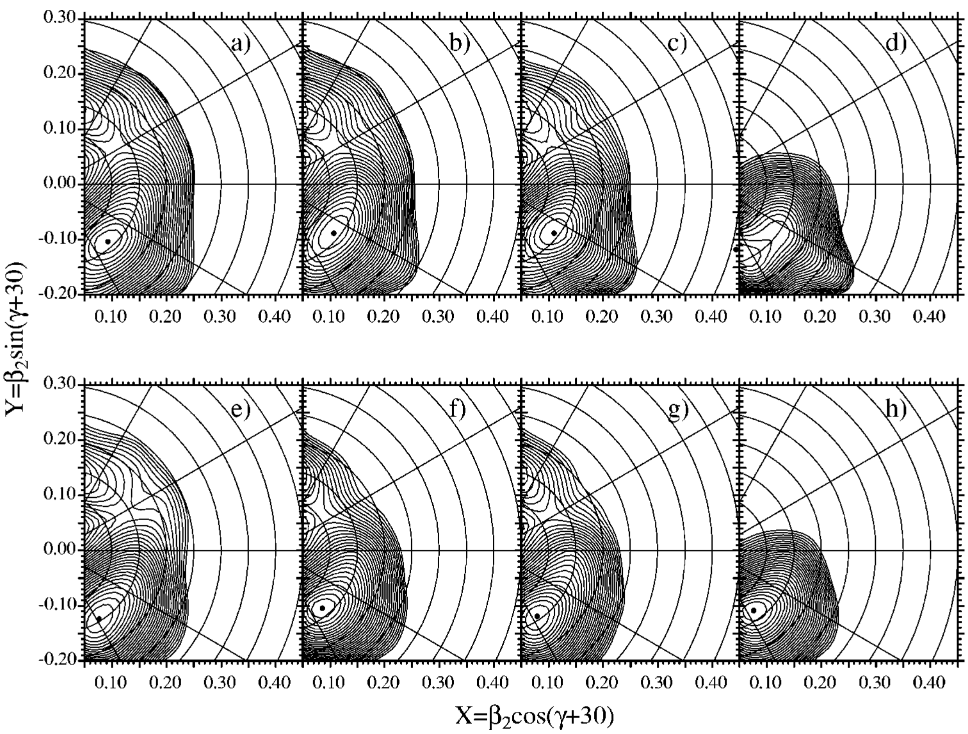

FIG. 6. TRS calculations for the following bands in ^{190}Au. (a) 11^- band, calculated at $\hbar\omega = 0.168$ MeV, (b) 12^- band at $\hbar\omega = 0.168$ MeV, (c) band (a) below the band crossing at $\hbar\omega = 0.207$ MeV, (d) band (a) above the band crossing at $\hbar\omega = 0.286$ MeV, (e) band (d) at $\hbar\omega = 0.207$ MeV, (f) band (e) at $\hbar\omega = 0.168$ MeV, (g) band (f) below the band crossing at $\hbar\omega = 0.168$ MeV, and (h) band (f) above the band crossing at $\hbar\omega = 0.286$ MeV.

Routhian of the 12^- band (favored signature), while the normal position is restored at higher rotational frequency. Signature inversion has also been found in a number of rare-earth odd-odd nuclei [23] and proved to be a phenomenon challenging the theoretical models. A study of the signature inversion in the doubly odd ^{186,188}Au nuclei has been done using CSM calculations [22], and it was shown that if a nonaxial shape with $\gamma \sim -70°$ is assumed, the *B* Routhians in ^{186,188}Au become yrast at low rotational frequency and a signature inversion takes place at a frequency of $\hbar\omega = 0.22$ MeV. This frequency, however, was much lower than the experimentally measured one of 0.35 MeV. It should be noted, though, that the signature inversion frequency is strongly dependent on the value of the γ deformation, thus a study of the nuclear shape is needed.

The CSM Routhians for the 11^- and 12^- bands in ^{190}Au corresponding to the nuclear deformations predicted by the TRS model, were constructed and are shown in the bottom panel of Fig. 5. Thus, the Routhian of the 11^- band was obtained as a sum of the *e* and *B* diabatic Routhians calculated for $\gamma = -80°$ and the Routhian of the 12^- band as a sum of the *e* and *A* Routhians calculated for $\gamma = -70°$. In good agreement with the experimental data, signature inversion is predicted by the calculations. Moreover, the value of the theoretical signature inversion frequency of 0.306 MeV is in excellent agreement with the experimentally measured one of 0.313 MeV. The precision of this prediction on a phenomenon that is so difficult to describe, is striking.

B. Band (a)

A band crossing takes place between the 17^- and 22^- levels in the yrast bands as indicated by the irregularity of the transition energies. This band crossing is associated with the alignment of a $\nu i_{13/2}$ pair along the rotational axis. Indeed, among the orbitals close to the Fermi level only the involvement of a $\nu i_{13/2}$ pair can reproduce the large aligned angular momentum of $\sim 21.5\hbar$ of band (a) (see Fig. 5). Furthermore, $\nu i_{13/2}$ nature is suggested for the first band crossing in the neighboring $^{190-194}$Hg [24], ^{190,192}Pt [25,26], and ^{187,189,191,193}Au [10,27–31] isotopes. Thus, a $\pi h_{11/2}^{-1} \otimes \nu i_{13/2}^{-3}$ configuration is assigned to band (a).

The TRS calculations predict a nuclear deformation with $\beta_2 = 0.14$, $\beta_4 = -0.027$, and $\gamma \sim -69°$ for band (a), as shown in panel (c) of Fig. 6. It is then expected that the three excited $i_{13/2}$ neutrons will occupy the three close lying (at this nonaxiality) *A*, *B*, and *C* Routhians and thus no sets of rotation-aligned bands will be observed. In excellent agreement with this prediction, only one sequence, band (a), is found experimentally above the first band crossing.

Very good agreement is also obtained for the alignments and band-crossing frequencies. The experimentally measured aligned angular momentum of $21.5\hbar$ of this band is in very good agreement with the predicted value of $21.0\hbar$ at $\gamma = -70°$. The experimental *BC* band-crossing frequency of 0.27 MeV is the same as the *BC* band-crossing frequency in the neighboring axially symmetric ^{191}Hg isotone of 0.266 MeV [24]. This observation is in very good agreement with the prediction that the *BC* band-crossing frequency does not change near the axially symmetric shape (see Table II).

The next band crossing in band (a) occurs around the 28^- level. In the neighboring ^{191}Hg isotone the *ABC* band is crossed by two bands, associated with the excitation of (i) two low-*j* ($j = p_{3/2}, f_{5/2}$) neutrons, and (ii) a $\nu h_{9/2}$ and a low-*j* neutron, respectively [21]. These two band crossings occur at a rotational frequency of $\hbar\omega \sim 0.45$ MeV and carry a gain in alignment of $\sim 2.2\hbar$ and $\sim 5\hbar$, respectively [21]. The experimental gain in alignment at the band crossing in ^{190}Au is $\sim 6\hbar$ and the alignment takes place at much lower rotational

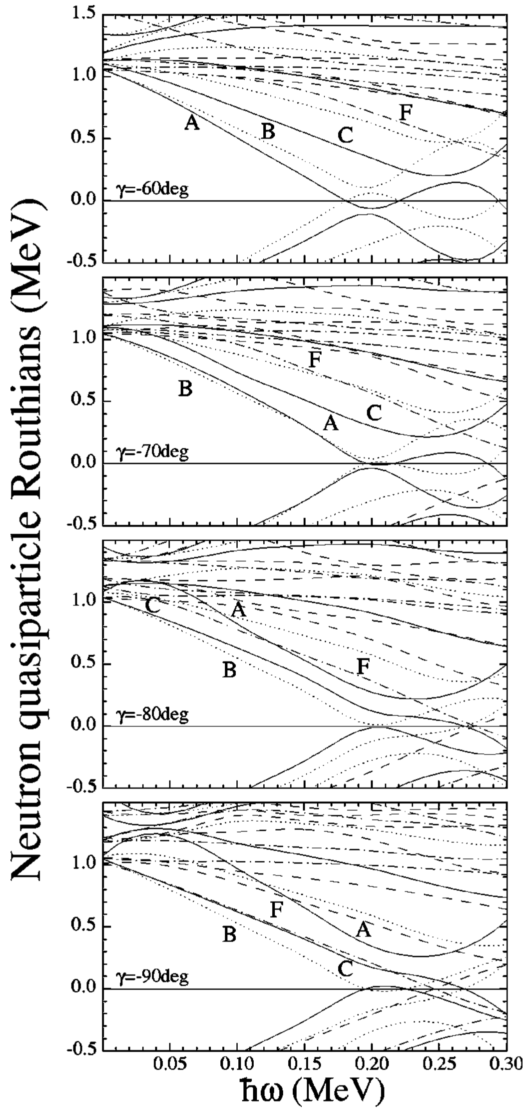

FIG. 7. Cranked shell model calculations for ^{191}Au performed for neutrons. A Woods-Saxon potential with universal parameters is used. Nuclear deformation of $\beta_2=0.136$ and $\beta_4=-0.027$ is chosen. The panels from top to bottom correspond to $\gamma=-60°$, $-70°$, $-80°$, and $-90°$. The Routhians with $(\pi,\alpha)=(+,+1/2)$ are represented with a solid line, $(+,-1/2)$ with a dotted line, $(-,+1/2)$ with a dash-dotted line, and $(-,-1/2)$ with a dashed line.

frequency of $\hbar\omega=0.35$ MeV. The TRS calculations predict that above this band crossing the nuclear shape becomes very triaxial with $\gamma\sim-100°$ [see panel (d) in Fig. 6], and that a gain in the neutron alignment of $\sim 8\hbar$ is expected. Thus, they predict that a $\nu h_{9/2}^{-2}$ (e.g., *EF*) excitation is more likely in ^{190}Au. The suggested different nature of this band crossing in ^{190}Au can be caused by the deformation driving properties of the odd $\pi h_{11/2}$, which induces rather large nonaxiality in the nuclear shape of Au isotopes, and thus the low-*K* orbitals from the $\nu h_{9/2}$ shell drop close to the Fermi level (see Fig. 7).

C. Bands (d), (e), and (f)

The 20^+ isomer is assigned to the $\pi h_{11/2}^{-1}\otimes\nu i_{13/2}^{-2}h_{9/2}^{-1}$ configuration by considering the orbitals closest to the Fermi level and the systematics of configuration assignments in this mass region [18]. Thus, the sequences (d), (e), and (f) in ^{190}Au are associated with a set of rotation-aligned bands, similar to the bands above the $31/2^+$ isomer in the neighboring ^{191}Au isotope [10].

For the expected γ deformation of $\sim-90°$ the calculations predict the presence of a set of rotation-aligned bands corresponding to the *eFAB*, *eFAC*, and *eFBC* configurations. In excellent agreement with these predictions three sequences, (d), (e), and (f), are observed, two with signature of $\alpha=0$ and one with $\alpha=1$. Considering the signatures and alignments, band (d) is assigned to the *eFBC* configuration, while bands (e) and (f) are assigned to *eFAC* and *eFAB* configurations, respectively.

The TRS calculations performed for the three sequences showed large nonaxial deformation with $\beta_2=0.14$ and $\gamma\sim -88°$, $-81°$, and $-86°$ for the (d), (e), and (f) sequences, respectively [see panels (e), (f), and (g) in Fig. 6]. Excellent agreement with the theoretical predictions is found for the aligned angular momenta of these bands. The experimental alignments of $19.5\hbar$, $20.0\hbar$, and $20.5\hbar$ for the bands (d), (e), and (f) (see Fig. 5) are similar to the theoretical values of $19.8\hbar$, $19.8\hbar$, and $21.0\hbar$ for $\gamma=-90°$, $-80°$, and $-90°$ respectively (see Table II). Taking into account the strong dependence of the aligned angular momenta on the value of the γ deformation for such large nonaxiality, this good agreement is notable.

It is interesting to note that the experimental Routhian of band (f), *eFAB* configuration, lies at a higher excitation energy than that of the band (d), *eFBC* configuration, as shown in Fig. 5. This can be compared with the relative positions of the Routhians of the (a), (b), and (c) bands in the neighboring ^{191}Au nucleus, assigned to *eBC*, *eAB*, and *eAC* configurations respectively, where the Routhian of band (b) lies at the lowest excitation energy [10]. Furthermore, a gradual increase in the experimental alignment of band (d) is observed in ^{190}Au (see Fig. 5). It should be taken into account, however, that only a small nonaxial deformation of $\gamma\sim-70°$ was predicted for the (a), (b), and (c) bands in ^{191}Au, while in ^{190}Au (due to the involvement of the *F* Routhian) the nuclear shape is largely nonaxial. As a consequence, the interaction of the *A* and *C* Routhians, which takes place at $\hbar\omega \sim 0.1$ MeV for $\gamma=-70°$ is delayed and occurs at larger rotational frequencies, $\hbar\omega\gtrsim 0.20$ MeV for $\gamma=-90°$, for which the rotational bands are already present (see Fig. 7). Therefore, it is likely that this interaction is causing a strong mixing of the *A* and *C* Routhians in the configurations of the (d) and (f) bands in ^{190}Au and is probably the reason for the observed relative position of the Routhians and the increase in the alignment of band (d). The experimental Routhians of the (d), (e), and (f) bands are found to lie very close to the Routhian of band (a) (see Fig. 5). This observation is in excellent agreement with the theoretical predictions that only at very large nonaxiality of $\gamma\sim-90°$ the *F* Routhian drops close to the Fermi surface and successfully competes with the positive parity Routhians (see Fig. 7).

An alignment of two $i_{13/2}$ neutrons occurs in the (f) sequence around the 30^+ level. It is indicated by the large gain in the aligned angular momentum and takes place at a rotational frequency of 0.33 MeV (see Fig. 5). *CD* excitations

TABLE II. CSM alignments, calculated at $\hbar\omega = 0.30$ MeV, and band-crossing frequencies, for different γ deformations in ^{190}Au. Information on the labeling convention is also included.

			−60°	−70°	−80°	−90°	−100°
Alignments ($\hbar$)							
A	$(+,+)$	$\nu i_{13/2}$	6.23	6.26	6.15	5.97	5.78
B	$(+,-)$	$\nu i_{13/2}$	5.16	5.26	5.35	5.40	5.45
C	$(+,+)$	$\nu i_{13/2}$	4.11	4.25	4.28	4.72	5.18
D	$(+,-)$	$\nu i_{13/2}$	3.05	3.14	3.22	3.24	3.42
E	$(-,-)$	$\nu h_{9/2}$	2.74	3.06	3.11	3.29	3.39
F	$(-,+)$	$\nu h_{9/2}$	3.85	3.98	4.04	4.25	4.38
e	$(-,-)$	$\pi h_{11/2}$	5.01	5.21	5.33	5.40	5.46
$\hbar\omega_c$ (MeV)							
AB			0.195	0.200	0.213	0.220	0.230
BC			0.245	0.240	0.227	0.215	0.215
AD			0.255	0.263	0.275	0.288	0.310
CD			0.340	0.323	0.310	0.307	0.310
EF			0.477	0.407	0.358	0.305	0.270

with similar gain in the aligned angular momentum and band-crossing frequencies are known in the neighboring even Hg and odd Au nuclei [10,27–30]. The TRS calculations predict that above this band crossing the nuclear shape of ^{190}Au remains nonaxial with $\gamma \sim -85°$ (see Fig. 6). The measured experimental alignment of 29.5$\hbar$ for this band is in good agreement with the predicted value of 29.0$\hbar$ for $\gamma = -90°$. It should be noted that the alignments of a second $i_{13/2}$ neutron pair in the neighboring ^{192}Hg and ^{191}Au nuclei were associated with smaller nonaxiality. An axially symmetric oblate shape was assumed for ^{192}Hg (for *ABCD* configuration) [24] and nonaxial shape with $\gamma \sim -70°$ was predicted for ^{191}Au (*eABCD* configuration) [10]. In excellent agreement with the predictions that the *CD* band-crossing frequency is decreasing at larger nonaxiality (see Table II), experimental values of 0.36, 0.34, and 0.33 MeV were found in ^{192}Hg [24], ^{191}Au [10], and ^{190}Au, respectively.

An alignment of two $i_{13/2}$ neutrons is probably also taking place in the (d) sequence above the 26^+ level, as shown by the gain in the aligned angular momentum. An *AD* band crossing seems to be most likely and therefore the (d) sequence (*eFBC* configuration) should be fed by the higher energy levels of the (f) sequence (*eFABCD* configuration). Indeed, in very good agreement with these considerations, such connection between the 30^+ levels of the (f) and (d) sequences was experimentally observed. In addition, band (d) is fed by two other paths, the nature of which remains unclear.

Thus, the predictions of the TRS and CSM calculations for the presence, alignments, band-crossing frequencies, and signature splitting in the sets of rotation-aligned bands in ^{190}Au were found to be in very good agreement with the experimental data. A study of the systematic trends in the nuclei in this mass region (like the dependence of the signature inversion frequency on the neutron number in the odd-odd Au nuclei, the decreasing signature splitting in the $\pi h_{11/2}^{-1} \otimes \nu i_{13/2}^{-2}$ bands in the $A=190$ odd-even Au nuclei with increasing neutron number, etc.) may be able to reveal further details of the nature of these bands.

D. Structures (b), (c), (g), and (h)

Structure (c) is based on the 23^- level at 3460 keV and looks very similar to the irregular structure (f) in the neighboring ^{191}Au nucleus [10]. We thus suggest a similar configuration of $\pi h_{11/2}^{-1} \otimes \nu i_{13/2}^{-3} h_{9/2}^{-1} j$, $j=(p_{3/2}, f_{5/2})$. The decay of the 23^- level towards structures associated with the excitations of $\nu i_{13/2}$ and $\nu h_{9/2}$ gives further support for such a configuration assignment. The energy of the 23^- level, 3460 keV, is also consistent with the sum (3771 keV) of the energies of the 20^+ isomeric level and the 15^+ bandhead of the semidecoupled bands. Similar to ^{191}Au, structure (b) might be associated with the same $\pi h_{11/2}^{-1} \otimes \nu i_{13/2}^{-3} h_{9/2}^{-1} j$ quasiparticle configuration, but involving the unfavored sequence of the semidecoupled bands.

The structure (g) seems to be more irregular and is probably similar to the transitions observed above the $37/2^+$ level in the ^{187,189,191}Au nuclei [10,27–30]. It may have noncollective nature.

The 15^+ level at 1599 keV has been associated with the onset of the semidecoupled bands in ^{190}Au and assigned to the $\pi h_{11/2}^{-1} \otimes \nu i_{13/2}^{-2} j$, $j=(p_{3/2}, f_{5/2})$ configuration [8]. The identification of the 20^+ isomer at 2172 keV allows the separation of the structures associated with this isomer [18] and thus the sequences labeled (h) are suggested to belong to the semidecoupled bands in ^{190}Au. In the Au isotopes these bands are considerably weaker than in the Hg and Pt isotopes. Such a difference in the population pattern is most likely due to the deformation driving properties of the odd $h_{11/2}$ proton, which induces nonaxial shapes in the Au isotopes, and causes the $\nu h_{9/2}$ orbitals to drop much closer to the Fermi level. Thus the structures involving such orbitals (like the structures above the 20^+ and 23^- levels in the odd-odd and above the $31/2^+$ and $39/2^-$ levels in the odd-even Au isotopes) become yrast.

V. CONCLUSION

In summary, the level scheme of ^{190}Au was extended up to high spin using two complementary experiments. The ^{186}W(^{11}B, $7n$) reaction and the Eurogam-II γ spectrometer was used in the first experiment. The ^{186}W(^{11}B, $5n$) reaction and the electron spectrometer of Orsay coupled to eight Eurogam-I Ge detectors was used in the second, internal conversion spectroscopy, experiment. The data analysis included γ coincidence, angular distribution, linear polarization, internal conversion coefficient, and lifetime measurements. Several rotational bands were found and were associated with high-j low-K configurations. Since the properties of these bands often strongly depend on the predicted magnitude of the nonaxiality of the nuclear shape, they can be used as a test of the theoretical models. Several properties of these bands in ^{190}Au, such as the presence of sets of rotation-aligned bands, band-crossing frequencies, alignments, and signature inversion frequency, were compared with the experimental data from the neighboring axially symmetric ^{191}Hg and nonaxial ^{191}Au, as well as with the corresponding theoretical predictions of the TRS and CSM models. Very good agreement was obtained between the experimental measurements and the theoretical calculations, thus supporting the predictions for nonaxial deformations with $-90° \leqslant \gamma \leqslant -70°$. It seems that a systematic study of the nuclei in this mass region may be able to reveal further details of the nature of these nonaxial nuclei.

ACKNOWLEDGMENTS

The EUROGAM project was funded jointly by the IN2P3 (France) and the EPSRC (UK). We are grateful to H. Folger and his collaborators at the GSI Target Laboratory for their high quality targets and to the teams of the Vivitron (IReS, Strasbourg) and IPN Tandem (Orsay) for providing excellent beams. Fruitful discussions with M.-G. Porquet are acknowledged.

[1] R. Bengtsson, T. Bengtsson, J. Dudek, G. Leander, W. Nazarewicz, and J. Zhang, Phys. Lett. B **183**, 1 (1987).
[2] W. Nazarewicz, M. A. Riley, and J. D. Garett, Nucl. Phys. **A512**, 61 (1990).
[3] Th. Hilberath, St. Becker, G. Bollen, H.-J. Kluge, U. Krönert, G. Passler, J. Rikovska, R. Wyss, and the ISOLDE Collaboration, Z. Phys. A **342**, 1 (1992).
[4] J. Rikovska, R. Wyss, and P. B. Semmes, Hyperfine Interact. **75**, 59 (1992).
[5] L. Esser, U. Neuneyer, R. F. Casten, and P. von Brentano, Phys. Rev. C **55**, 206 (1997).
[6] *Table of Isotopes*, edited by R. B. Firestone and V. S. Shirley, 8th ed. (Wiley, New York, 1996), and references therein.
[7] J. Meyer-ter-Vehn, Nucl. Phys. **A249**, 111 (1975); **A249**, 141 (1975).
[8] A. Neskakis, R. M. Lieder, H. Beuscher, Y. Gono, D. R. Haenni, and M. Müller-Veggian, Nucl. Phys. **A390**, 53 (1982).
[9] H. Toki, H. L. Yadav, and A. Faessler, Z. Phys. A **292**, 79 (1979).
[10] E. Gueorguieva, C. Schück, A. Minkova, Ch. Vieu, F. Hannachi, M. Kaci, M.-G. Porquet, R. Wyss, J. S. Dionisio, A. Korichi, and A. Lopez-Martens, Phys. Rev. C **68**, 054308 (2003).
[11] R. Wyss, W. Satula, W. Nazarewicz, and A. Johnson, Nucl. Phys. **A511**, 324 (1990).
[12] W. Nazarewicz, G. A. Leander, and J. Dudek, Nucl. Phys. **A467**, 437 (1987).
[13] J. Dudek, Z. Szymański, and T. Werner, Phys. Rev. C **23**, 920 (1981).
[14] G. Duchêne *et al.*, in *Proceedings of the Workshop on Large Gamma-Ray Detector Arrays, Chalk River, Canada, 1992*, AECL Report No. 10613, pp. 359, 364; G. Duchene *et al.*, Nucl. Instrum. Methods Phys. Res. A **432**, 90 (1999).
[15] P. M. Jones, L. Wei, F. A. Beck, P. A. Butler, T. Byrski, G. Duchêne, D. de France, F. Hannachi, G. D. Jones, and B. Kharraja, Nucl. Instrum. Methods Phys. Res. A **362**, 556 (1995).
[16] C. Schück *et al.*, Phys. Rev. C **56**, R1667 (1997).
[17] E. Gueorguieva, M. Kaci, C. Schück, A. Minkova, Ch. Vieu, J. J. Correia, and J. S. Dionisio, Nucl. Instrum. Methods Phys. Res. A **474**, 132 (2001).
[18] E. Gueorguieva *et al.*, Phys. Rev. C **64**, 064304 (2001).
[19] J. S. Dionisio *et al.*, Nucl. Instrum. Methods Phys. Res. A **362**, 122 (1995).
[20] Ts. Venkova *et al.*, KFA report, 1994 (unpublished).
[21] D. Ye *et al.*, Nucl. Phys. **A537**, 207 (1992).
[22] V. P. Janzen *et al.*, Phys. Rev. C **45**, 613 (1992).
[23] Y. Liu, Y. Ma, H. Yang, and S. Zhou, Phys. Rev. C **52**, 2514 (1995).
[24] H. Hübel, A. P. Byrne, S. Ogaza, A. E. Stuchbery, G. D. Dracoulis, and M. Guttormsen, Nucl. Phys. **A453**, 316 (1986).
[25] J. C. Cunnane, M. Piiparinen, P. J. Daly, C. L. Dors, T. L. Khoo, and F. M. Bernthal, Phys. Rev. C **13**, 2197 (1976).
[26] S. A. Hjorth, A. Johnson, Th. Lindblad, L. Funke, P. Kemnitz, and G. Winter, Nucl. Phys. **A262**, 328 (1976).
[27] C. Bourgeois, M.-G. Porquet, N. Perrin, H. Sergolle, F. Hannachi, G. Bastin, and F. Beck, Z. Phys. A **333**, 5 (1989).
[28] J. K. Johansson, D. G. Popescu, D. D. Rajnauth, J. C. Waddington, M. P. Carpenter, L. H. Courtney, V. P. Janzen, A. J. Larabee, Z. M. Liu, and L. L. Riedinger, Phys. Rev. C **40**, 132 (1989).
[29] C. Bourgeois, A. Korichi, N. Perrin, D. G. Popescu, F. Azaiez, D. Hojman, H. Sergolle, and G. Bastin, Z. Phys. A **343**, 243 (1992).
[30] Ts. Venkova *et al.*, Z. Phys. A **344**, 231 (1992).
[31] V. Kölschbach, P. Schüler, K. Hardt, D. Rosendaal, C. Günther, K. Euler, T. Tölle, M. Marten-Tölle, and P. Zeyen, Nucl. Phys. **A439**, 189 (1985).